Journal of Materials Chemistry A

ROYAL SOCIETY OF CHEMISTRY

PAPER

View Article Online
View Journal | View Issue

Cite this: *J. Mater. Chem. A*, 2020, **8**, 13610

Pressure-driven chemical lock-in structure and optical properties in Sillen compounds $PbBiO_2X$ (X = Cl, Br, and I)†

Qian Zhang,[a] Xuqiang Liu,[a] Nana Li,[a] Bihan Wang,[a] Quan Huang,[b] Lin Wang,[a] Dongzhou Zhang,[c] Yonggang Wang *[a] and Wenge Yang *[a]

Received 23rd March 2020
Accepted 15th June 2020

DOI: 10.1039/d0ta03291c

rsc.li/materials-a

Sillen compounds with the general formula of $PbBiO_2X$ (X = Cl, Br, I) are frequently studied as photocatalysts, and have attracted widespread attention due to their degradation of organic contaminants and water oxidation under visible light irradiation. Among many photoelectric materials, the band gap has been reduced approaching to the optimum value by pressure (1.34 eV for photovoltaic materials according to the Shockley–Queisser limit), which is favorable to their photo-responsive applications. However, such enhanced properties are usually restored after the pressure is released. Here, by combining the pressure and chemical engineering tools, we discovered that the optimized structure and optical band gap of $PbBiO_2Br$ could be locked after compression–decompression treatment cycling by selecting appropriate elemental species. The pressure-induced strain retention in $PbBiO_2Br$ could be the cause of the structural and optical irreversible behavior. Moreover, the compression behavior and optical band gap under high pressure in the $PbBiO_2X$ system were studied systematically by *in situ* high pressure synchrotron X-ray diffraction, UV-vis absorption spectroscopy and resistivity experiments. Along with the enhanced photocurrent under compression, the $PbBiO_2X$ compounds under external pressure exhibited great potential for photocatalytic applications under solar light irradiation. In a suitable element category, the pressure-driven structural lock-in preserves its optical performance, opening up a new window for manipulating and filtrating better multifunctional materials.

Introduction

The mixed-anion compound beyond one anionic species in a single phase offers an opportunity to design and control novel physical and chemical properties due to the flexibility of its semiconductor structure and composition.[1] In particular, bismuth-containing semiconductors afford many potential applications in thermoelectric,[2–5] ferroelectric[6–9] and photocatalytic fields,[10–18] owing to the stereoactive $6s^2$ configuration of Bi, as well as the modulated crystal/electronic structure by mixed anions with its distinct electronegativity. For example, the oxyselenide BiCuSeO crystallizes in a regular stack of conductive $[Cu_2Se_2]$ sheets and insulating $[Bi_2O_2]$ sheets. In favor of its layered structure, the intrinsic low thermal conductivity (0.60 W m^{-1} K^{-1} at room temperature) and the narrow band gap (~0.8 eV) make it a promising candidate for the highly efficient thermoelectric application.[4,5] It was found that some Bi-based oxyhalide Aurivillius compounds also adopted an intergrowth of fluorite-like $[Bi_2O_2]$ and perovskite-like $[A_{n-1}B_nO_{3n+1}]$ units, such as Bi_4NbO_8Cl, Bi_4TaO_8Cl, and $Bi_3Pb_2Nb_2O_{11}Cl$. Their ferroelectricity was widely studied, owing to their polar structure, although the neutron diffraction revealed that a ferroelectric-type phase transition occurred at high temperature from an ideal tetragonal to orthorhombic or pseudo-tetragonal structure.[8,9] In addition, some other closely related layered oxyhalides, such as the Sillen family, exhibited excellent photocatalytic properties.[18] Under solar light irradiation, they were reported to achieve organic pollutant decomposition,[14,15] wastewater purification, and water oxidation.[17,19] So far, the chemical strategies for approaching better performance on the layered Bi-based semiconductors are primarily dedicated to the composition and morphology engineering, all of which are subjected to the fabrication process.

[a]*Center for High Pressure Science and Technology Advanced Research (HPSTAR), Shanghai 201203, China. E-mail: yangwg@hpstar.ac.cn; yonggang.wang@hpstar.ac.cn*

[b]*College of Material and Chemical Engineering, Zhongyuan University of Technology, Zhengzhou 450007, China*

[c]*Hawaii Institute of Geophysics & Planetology, University of Hawaii Manoa, Honolulu, Hawaii 96822, USA*

† Electronic supplementary information (ESI) available: Diffuse reflectance spectra of $PbBiO_2X$ at ambient condition, XRD patterns of $PbBiO_2Br$ and $PbBiO_2I$ at different pressures, GSAS refinement results for $PbBiO_2X$, bonding distance and angle changes with pressure, pressure dependence of resistivity of $PbBiO_2I$. See DOI: 10.1039/d0ta03291c

Pressure, as an alternative approach to modify physical/chemical properties in modern material science, has been proven as a clean efficient route to tune the crystal structure and electronic configuration for photoelectric materials.[20–22] Recently, it has been reported that with an applied external pressure, the bismuth oxyhalide BiOCl suffered from a redistribution of the Bader charge among its component ions. A following isostructural phase transition was experimentally noticed, as proved by the abnormal lattice compression (c/a) within the pressure range from 15.1 GPa to 22.1 GPa.[23] Our previous pressure response studies on bismuth oxychalcogenides have also demonstrated a steady anisotropic lattice contraction upon compression. Due to the pressure-induced competition between the charge delocalization and band gap opening, the electrical resistivity rollback was observed beyond 12 GPa.[24] All these findings encourage us to gain deep insight into the structure–properties relationship for other Bi-based mixed anion compounds under high pressure, which has been rarely reported so far.

Sillen X compounds are typical layered semiconductors with single/multiple layers of X atom intercalated in between the fluorite-like Bi_2O_2-based layers.[25,26] With a single halogen atom layer insertion, $PbBiO_2X$ (X = Cl, Br, I) exhibits potential visible-light-responsive photocatalytic activities in water oxidation or the degradation of organic pollutants due to its appropriate band levels.[17,27] In this work, by selecting the series X species (X = Cl, Br, I), we conducted the *in situ* comparison studies on the structure and optical property under high pressure with synchrotron X-ray diffraction and optical absorption methods. For the first time, we discovered the band-gap narrowing for all of them during compression, but only $PbBiO_2Br$ retained a partially high pressure structure and property upon decompression. The narrowed band-gap for the pressurized $PbBiO_2Br$ got closer to the pristine $PbBiO_2I$, which has the narrowest band-gap among these three compounds. From our results, the external pressure could be used as a great potential tool towards better semiconducting materials with engineered band gaps through the irreversible pressure-induced phase transformation. The abnormal structural, optical and transport behaviors of $PbBiO_2X$ could be achieved by combining the chemical and pressure efforts together.

Experimental details

Sample syntheses

As the precursor to synthesize the target $PbBiO_2X$ (X = Cl, Br, and I) samples *via* a two-step procedure, the particulate BiOX reactants were initially prepared by a co-precipitation method as follows: $Bi(NO_3)_3 \cdot 5H_2O$ (Aladdin, 99.0%) was added slowly into a solution containing stoichiometric amounts of NaCl (Rhawn, 99.5%), NaBr (Rhawn, 99.5%), and KI (Rhawn, 98.5%) respectively, with the Bi : X molar ratio of 1 : 1. The mixture was stirred at room temperature for 0.5 hour in air and washed with distilled water and ethanol, followed by drying at 60 °C for 10 hours. During the process of $PbBiO_2X$, the well-mixed powders of BiOX and PbO (Aladdin, 99.5%) with the stoichiometric proportion were calcined at 700 °C for 24 hours in alumina crucibles. The phase identification of the obtained products was carried out on an XPert Powder (analytical) X-ray diffractometer (XRD) with Cu Kα radiation.

High-pressure characterizations

Symmetrical diamond anvil cells (DAC) with 300 μm culet-size anvils were employed in all high-pressure experiments, which could facilely generate pressure beyond 50 GPa. T301 stainless steel foils were pre-indented to 50 μm in thickness, where the cavities were drilled by infrared laser with 150 μm-diameter. All fine-grinding powders were pressed into pellets with about 10 μm in thickness, and then loaded into the above cavities together with small ruby balls. In this way, ruby was used to calibrate the pressure by the luminescence method. Silicone oil was added in the cavities to serve as the pressure-transmitting medium to provide a quasi-hydrostatic pressure environment. The *in situ* high-pressure angle-dispersive XRD experiments were carried out at the 13 BM-C station of GSECARS at the Advanced Phonon Source (APS), in Argonne National Laboratory (ANL). A monochromatic X-ray beam (λ = 0.4340 Å) was focused to 15 μm in diameter (FWHM) in our diffraction experiments.[28] Two-dimensional diffraction patterns were recorded on a charge-coupled device (CCD) detector. The LaB_6 standard powder was used to calibrate the distance between sample and detector and the orientation parameters of the detector. The diffraction patterns were integrated using the program Dioptas.[29] It is worth noting that the silicone oil can provide a reasonable quasi-hydrostatic pressure environment below 15 GPa, which may introduce the pressure gradient inside the sample chamber, especially at the high-pressure region. Typically, the pressure variation was less than 0.2 GPa, and no more than 0.5 GPa above 15 GPa. The crystal structures were refined with the Rietveld method by using the General Structure Analysis System (GSAS) program packages.[30] *In situ* high-pressure optical measurements were performed on an UV-vis absorption spectrophotometer with the acquisition time of 2 s at room temperature (RT). Each reference was collected on the sample-free area with the same grating size and exposure time. The optical band gap was determined from the Tauc plot, a linear dependence for $(\alpha dh\nu)^2$ *versus* energy $h\nu$, where α is the absorption coefficient, d is the sample thickness, and h and ν are Planck's constant and frequency, respectively. The resistance measurements under high pressure were carried out by using the four-probe method, which was described in detail previously.[24] The resistivity was calculated by the Van der Pauw equation.[31] For the photocurrent measurements, a Zahner IM6 electrochemical workstation was utilized to record the I–t data by applying a constant bias voltage of 1 V. A 500 W Xenon lamp was utilized as the irradiation source (~5 mW cm^{-2} on the sample). The photo response measurements were monitored in the dark and under illumination in the DAC devices.

Results and discussion

Syntheses and crystal structures of $PbBiO_2X$

As typical Sillen X compounds, they were composed of a single halide anion [X] slab sandwiched by two-dimensional (2D) edge-

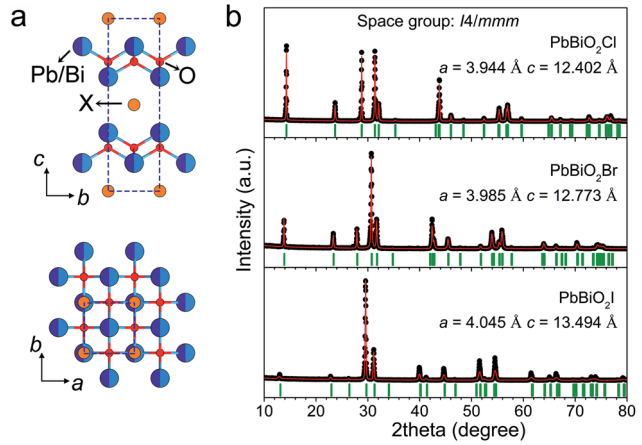

Fig. 1 Crystal structures of $PbBiO_2X$ (X = Cl, Br, I). (a) The tetragonal structure viewed along [100] and [001]. (b) Rietveld refinement results of the $PbBiO_2X$ samples with space group *I*4/*mmm*. In (b), experimental: black circle; simulation: red lines; Bragg reflections: olive bars.

shared $O(Bi/M)_4$ tetrahedra units.[26] The introduction of the aliovalent cations offers even broader opportunities for the original structural topologies based on the OBi_4 units. $CaBiO_2Cl$, $SrBiO_2X$ and $BaBiO_2X$ adopted monoclinic ($P2_1/m$) and orthorhombic (*Cmcm*) unit cells, where Bi was partially replaced by an alkaline earth metal.[11] Here, Bi is partially replaced by Pb with the same stereoactive $6s^2$ lone pair configuration.[25] The natural mineral perite $PbBiO_2Cl$ was reported to crystallize in the orthorhombic structure. However, our XRD examinations showed three profiles of $PbBiO_2X$ matching well with the standard powder diffraction files (PDF #39-0802, PDF #38-1008, PDF #78-0521) with the same tetragonal symmetry *I*4/*mmm*, as shown in Fig. 1. As the ionic size increased from Cl to I, both lattice *a* and *c* were expanded and the *c*/*a* ratio increased, since the X ion layers were intercalated between the $(Bi/Pb)_2O_2$ layers without changing these layers. The refined lattice parameters are: $a = 3.944$ Å, $c = 12.402$ Å for chloride, $a = 3.985$ Å, $c = 12.773$ Å for bromide, and $a = 4.045$ Å, $c = 13.494$ Å for iodide. Tiny deviations of less than 0.2% agreed well with the report by Ketterer *et al.* on them.[25]

Reversible/irreversible optical property evolution

Hydrostatic pressure can greatly affect the physical/chemical properties of functional materials, including the band gap adjustment. In order to track the optical behavior response to the external pressure, we performed the UV-vis absorption measurements on $PbBiO_2X$ at various pressures. At ambient pressure, $PbBiO_2X$ displayed steep absorption edges at about 517 nm, 538 nm and 563 nm (Fig. S1†) from X = Cl, Br and I, respectively, which are consistent with previous studies.[12,14,17,27] As the pressure increased, we noticed a piezochromic transformation for chloride from a translucent yellow to dark red, and eventually opaque red at 43 GPa (Fig. 2a). Accordingly, the absorption edges of all samples maintained were gradually redshifted throughout the compression process. The slope of absorbance at the edge tends to be gentle, which could be associated with the evolution of the band structure, likely, a transformation from the direct to indirect band gap. Meanwhile, over the entire visible range, the absorption increased with increasing pressure. The Tauc plot analysis was achieved by extrapolating the linear portion of the $(\alpha dhv)^2$ *versus* energy *hv* plot, indicating a direct band gap of 2.76 eV, 2.64 eV and 2.34 eV from X = Cl, Br, I at the initial pressure point, as shown in Fig. 2c–e. Upon compression, the band gap suffered continuous reduction to 1.98 eV, 1.70 eV and 1.40 eV for $PbBiO_2Cl$, $PbBiO_2Br$, and $PbBiO_2I$, respectively, at the maximum pressure of about 43 GPa. The narrowed band gaps can be explained by the pressure-enhanced orbital coupling of Pb/Bi-6s and X-np. Compared with the band gap tuning range of 0.42 eV (from 2.76 eV to 2.34 eV) with the chemical replacement of X from Cl to I, the pressure effect is more significant to ~1 eV ($PbBiO_2Cl$: 2.76–1.98 eV, $PbBiO_2Br$: 2.64–1.70 eV, $PbBiO_2I$: 2.34–1.40 eV) over 43 GPa for each X species. This finding was also realized in other layered bismuth oxychalcogenides.[24,32,33] Upon decompression, the color of $PbBiO_2Cl$ returned to the original translucent yellow, and the absorption edge completely recovered. The more exotic fact is, after releasing the pressure, unlike chloride and iodide, bromide exhibited a partially retainable band gap of ~2.52 eV, which is ~4.5% less than that of the starting $PbBiO_2Br$ (Fig. 2f and g). The narrow band gap helps to absorb the solar energy more widely. As vital photo-response parameters, both absorption enhancement and band gap narrowing could harvest solar light more effectively.

The optical band gap evolution can be correlated with changes in the structure under pressure. Fig. 3a shows the typical synchrotron XRD patterns of $PbBiO_2Cl$ at selected pressures. All sharp XRD peaks of the samples can be well indexed into the space group *I*4/*mmm*. As the pressure increases, all the reflections shift to higher 2θ angles, indicating lattice contraction with pressure. No noticeable extra peaks suggest that the initial structure symmetry was retained at the elevated pressure up to 40.5 GPa, the highest pressure applied. A similar structural evolution can also be found for $PbBiO_2Br$ and $PbBiO_2I$ in Fig. S2.† Generally, the peak widths of XRD at high pressure increased, which were typically caused by non-hydrostatic stress and other factors involving the grain size reduction and the increased local stain.[34,35] However, the peaks (101) for $PbBiO_2Cl$ centered at around 6.62° at ambient pressure abnormally broadened at high pressure, as shown in Fig. 3b. Two-dimensional images showed that the line width of the (101) diffraction peak dissipated gradually with increasing pressure, rather than splitting (Fig. 3c). We deduced that the symmetry did not break here. By using the GSAS package to perform the Rietveld refinement on $PbBiO_2X$ with the same tetragonal structure under high pressure, good agreement factors could be obtained as shown in Fig. S3.†

The lattice parameters of $PbBiO_2X$ based on the Le Bail refinements method are plotted *versus* pressure in Fig. 4. The *c* to *a* ratio (*c*/*a*) first decreased markedly with pressure, and then showed a gentle variation as the pressure further increased. Under pressure, the compression of $PbBiO_2X$ was anisotropic with the soft direction along the *c*-axis. In particular, for $PbBiO_2I$, it reached a minimum (*c*/*a* dropped about 9.2% from

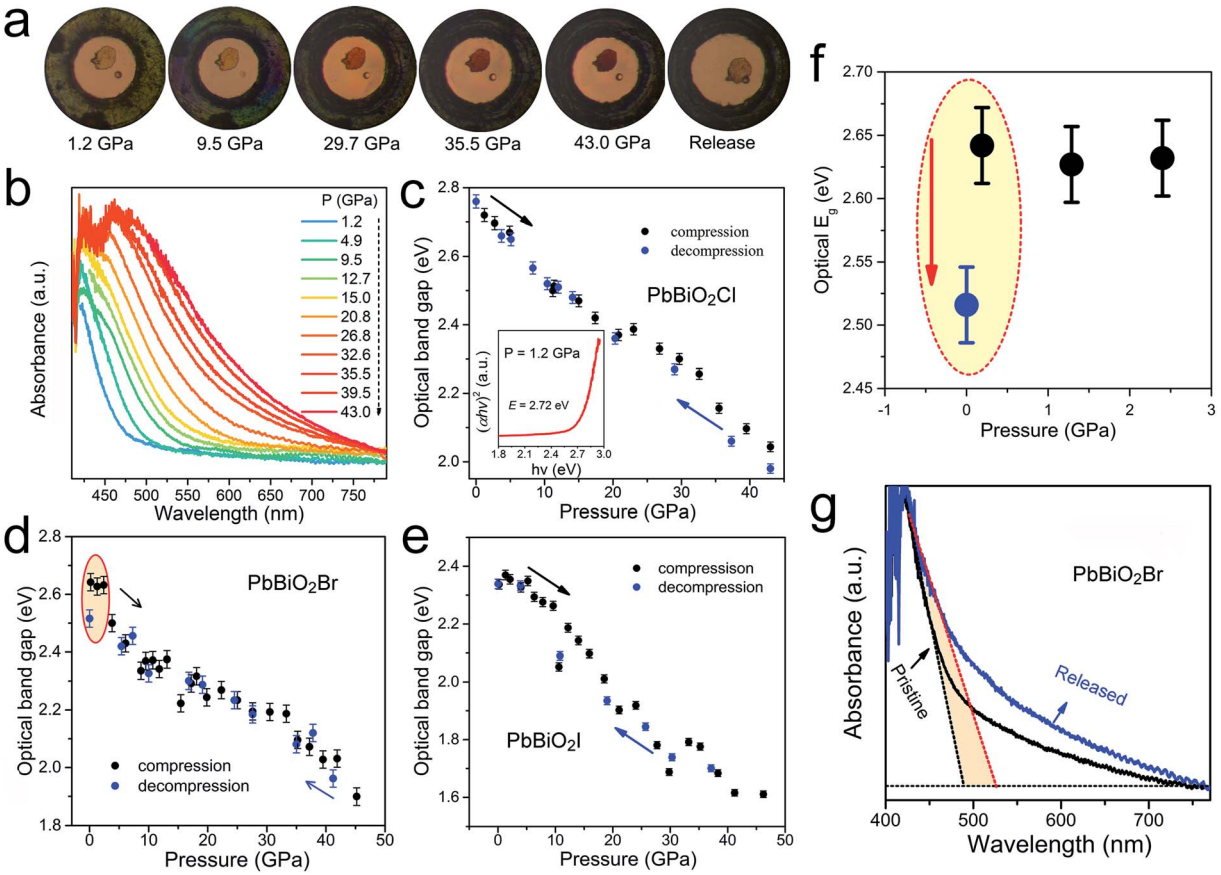

Fig. 2 (a) Optical microphotographs of $PbBiO_2Cl$ inside DAC during compression up to 43.0 GPa and decompression, displaying the piezochromic change from a translucent yellow to dark red. (b and c) Optical absorbance of $PbBiO_2Cl$ upon compression. The absorption edge redshifts with increasing pressure in $PbBiO_2Cl$. It recovered upon releasing the pressure. The inset gives the direct bandgap Tauc plots of the Kubelka–Munk function at 1.2 GPa for $PbBiO_2Cl$. The magnitudes of the band gaps can be estimated by extrapolating the linear portion of the Tauc plots to the baselines. (d and e) Pressure dependence of optical band gaps of $PbBiO_2Br$ and $PbBiO_2I$ upon both compression and decompression. (f) The bandwidth before and after compression for $PbBiO_2Br$. (g) Comparison of the absorbance before and after pressure treatment in $PbBiO_2Br$.

3.34 to 3.03) at 19.9 GPa. The abnormal relationship of *c*/*a versus* pressure for $PbBiO_2I$ could distinctly reflect the isostructural phase transition process, which has been proposed in many similar-layered compounds.[36,37] The more pressure-sensitive *c* axis shrinkage results from the considerable interspaces between the $(Bi/Pb)_2O_2$ layer and single X atom layer. The rigid *c*-axis for high pressure phase mainly arises from the stronger interlay Pb(Bi)-iodine bonding. Lattice *a* collapsed slightly at 17.9 GPa for chloride and 10.0 GPa for bromide, as shown in the inset, which we propose is an isostructural change. This mild lattice change could be associated with the evolution of the lone-pair electron configuration of bismuth upon compression. In $PbBiO_2X$, the Bi/Pb–O and Bi/Pb–Bi/Pb bonding distances were compressed with increasing pressure as shown in Fig. S4,† while the bonding angles for Bi/Pb–O–BiPb in the tetrahedron were distorted from 105.60°/117.52° to 103.79°/121.54°, which leads to the compression of the tetrahedral layer. With the non-oxygen anion from Cl to I, the $(Bi/Pb)_4O$ tetrahedron is different from the regular tetrahedron, which is attributed to the effect of the halogen atoms with different ionic radii. Next, we fitted the *V*–*P* curves of $PbBiO_2X$ with two sections over the entire pressure range by means of the third-order Birch–Murnaghan equation of state (EoS), as follows $P = \frac{3}{2}B_0\left[\left(\frac{V_0}{V}\right)^{7/3} - \left(\frac{V_0}{V}\right)^{5/3}\right] \times \left\{1 + \frac{3}{4}(B_0' - 4) \times \left[\left(\frac{V_0}{V}\right)^{3/2} - 1\right]\right\}$, where V_0 is the initial volume, and B_0' is the derivative of the bulk modulus with respect to pressure.[38] The isothermal bulk moduli B_0 were found to be 56(4) GPa, 53(3) GPa, and 43(3) GPa in the first pressure range for X = Cl, Br, and I, respectively. The reduced bulk module from chloride to iodide corresponds to an enhanced compressibility and decrease of elastic stiffness, as the anions changed from Cl to I. In the higher pressure range, B_0 was fitted as 88(3), 87(2), 98(8) GPa, which are much higher bulk moduli (about 60% higher) than those of the low-pressure phase.

In the Bi-based Sillen compounds, the lone-pair electrons play an important role in their photocatalysis application. The interaction between O-2p and Bi-6s can elevate the O-2p orbitals, favoring the redox reaction in the Bi-based

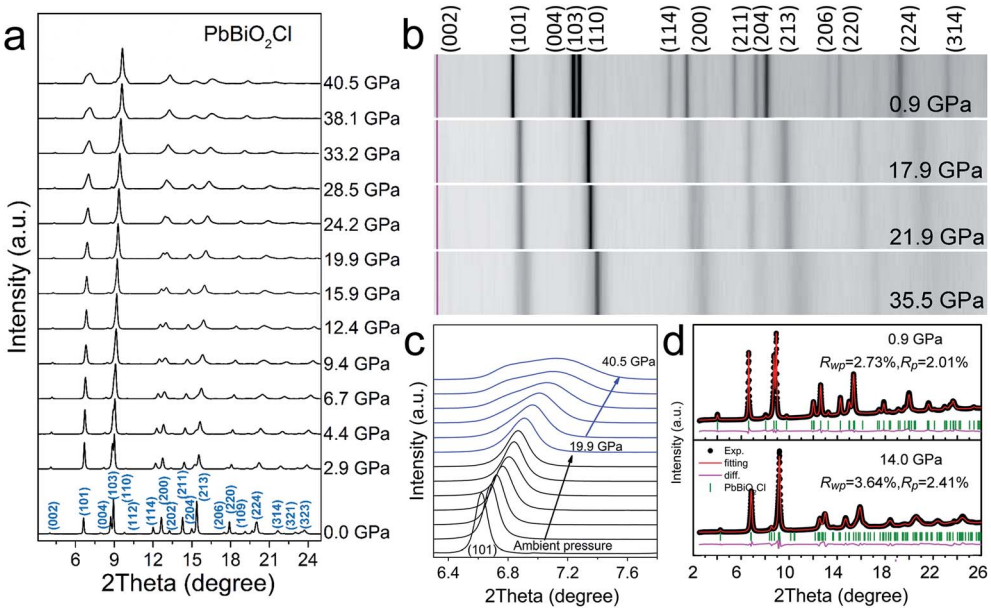

Fig. 3 Selected angle-dispersive XRD patterns of $PbBiO_2Cl$ with incident $\lambda = 0.4340$ Å at RT (a). (b) 2D images of $PbBiO_2Cl$ at 0.9 GPa, 17.9 GPa, 21.9 GPa and 35.5 GPa, respectively. (c) The evolution of (101) reflections under pressure. (d) Two refinement results for $PbBiO_2Cl$ at 0.9 GPa and 14 GPa.

photocatalyst.[39] The phenomenon follows the revised lone pair model proposed by Payne *et al.*[40] and Walsh *et al.*[41] Most photocatalysis research studies have shown the fact that lone pairs from post-transition metal cations (*e.g.*, Sn^{2+}, Sb^{3+}, Pb^{2+}, and Bi^{3+}) may improve the visible light-responsive photocatalysis efficiency in water splitting applications.[17] Under high pressure, Cheng *et al.* found that perovskite $PbCrO_3$ underwent an IPT at around 1.6 GPa, accompanying an insulator-metal transition. Based on the XANES measurements, they proposed that Pb-6s, 6p electrons are hybridized with Cr cations at the low-pressure phase. However, after the phase transition, the 6s electrons of Pb were restored to the lone pair state, which caused the insulating-to-metallic transport property change.[42] Here, we also observed the IPT in $PbBiO_2X$ and presumed it was associated with the pressure-driven lone pair electron configuration evolution. However, there is no conclusive evidence on the effect of the Bi lone pair on the compression behavior. It is indeed intriguing to clarify the role of the lone pair on the structure and properties at high pressure. A continuous development may be required.

Reversible/irreversible structural phase transition

XRD patterns before and after the compression–decompression cycle of $PbBiO_2X$ were then compared, as shown in Fig. 5a–c. The chloride and iodide analogs show good reversibility after pressure releasing. Surprisingly, the crystal structure of the pressure-released $PbBiO_2Br$ exhibits a partial retainable behavior. The XRD peaks from the pressure-released $PbBiO_2Br$ (even after 12 hours relaxation) shifted to a larger 2θ range than those of the pristine sample. In Fig. 5d, the enlarged XRD profiles from the hatched regions in Fig. 5c show clear differences between the pristine and pressure-released $PbBiO_2Br$ samples. The (002) peak shifted to a higher 2θ angle, along with the (110) and (103) peak merging for the decompressed $PbBiO_2Br$. By distinguishing them *via* peak fitting, it can be seen that the (103) peak shifts to a higher 2θ angle, while (110) almost completely recovers, meaning that the lattice constant c is largely not recovered due to the irreversible interlayer compression. The unit cell parameters for the pressure-released $PbBiO_2Br$ $a = 3.965(2)$ Å, $c = 11.863(3)$ Å, and $V = 187.9(3)$ Å^3 are smaller than the initial values ($a = 3.988(2)$ Å, $c = 12.774(3)$ Å, and $V = 203.2(4)$ Å^3). This drastically reduced c (7.1%), coupled with an almost totally recovered a-lattice (0.6% contraction), results in a volume reduction of 7.3%. The partially preserved crystal lattice could perfectly explain the abovementioned retainable optical band gap for $PbBiO_2Br$.

As an alternative approach, pressure can provide energy and tune samples away from its ground state, which allows the system to reach a metastable state with superior properties that could be preserved. Here, we plotted a hypothetical thermodynamic diagram of enthalpy for $PbBiO_2X$ in Fig. 5e. The black and red curves represent the compression and decompression enthalpy change as a function of pressure, respectively. The quenched state (red circle) is more energetically favored when the unit cell is more compressed in comparison to the initial state (black circle). From a thermodynamic point of view, the magnitude of the energy barrier depends on the detailed path of the structure transition. Liu *et al.*[43] reported the preserved structures and properties from high pressure treatment in hybrid perovskite $(BA)_2(MA)Pb_2I_7$, in which the Pb–I–Pb angle was closer to 180° after the compression and decompression process compared to the as-prepared sample, which enabled a better mixture of the Pb s and I p orbitals. The c-axis in the quenched $PbBiO_2Br$ was

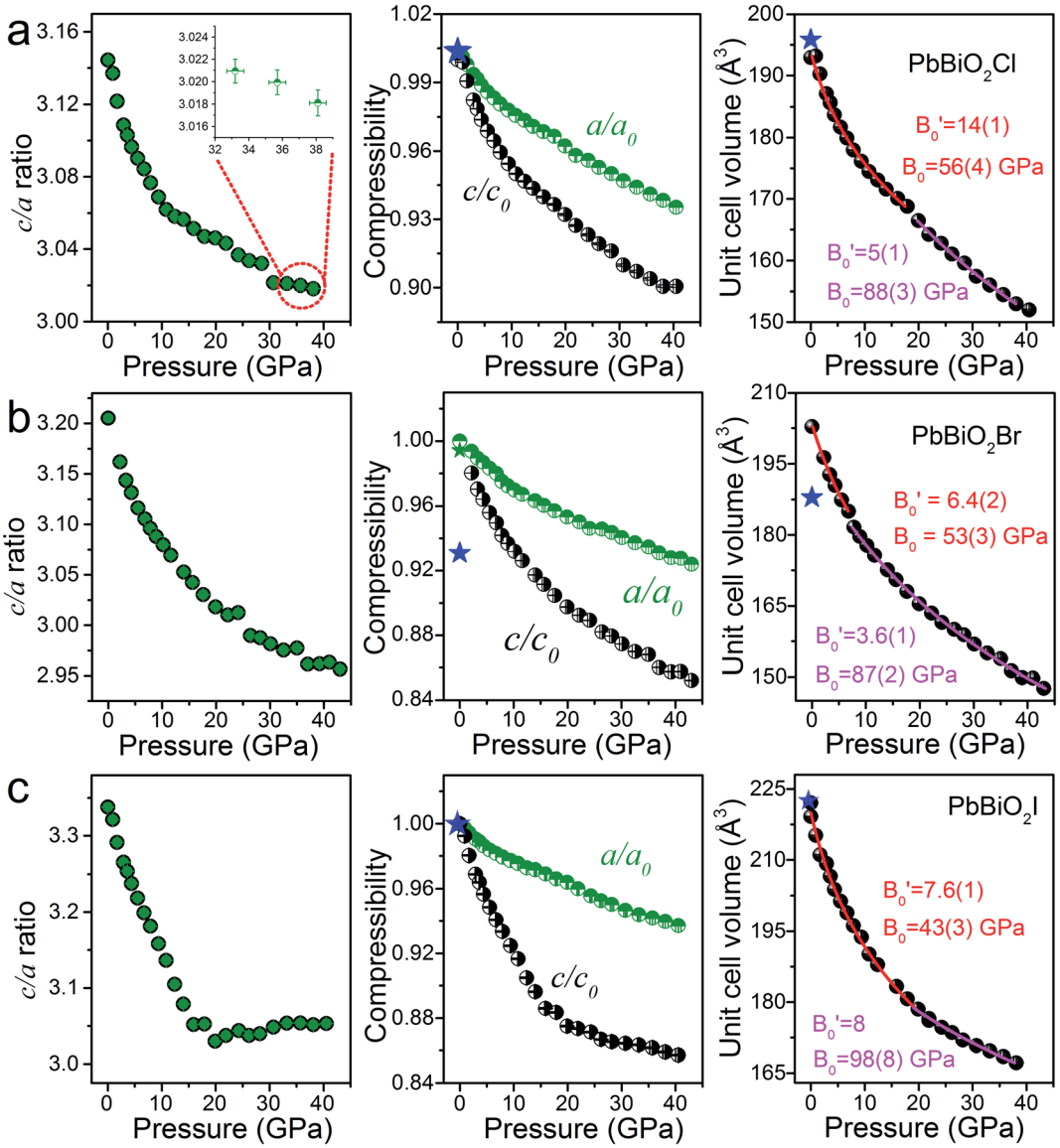

Fig. 4 Evolution of the lattice parameters c/a, the compressibility and unit cell volume of $PbBiO_2X$ as a function of pressure for: (a) $PbBiO_2Cl$, (b) $PbBiO_2Br$, and (c) $PbBiO_2I$. Red and pink lines are the EoS fitting results. Insets give the compressibility c/c_0 and a/a_0. The error bars, which come from the Rietveld refinement, are covered by the symbols. The enlarged view highlights the size of the c/a error lines for $PbBiO_2Cl$.

smaller than that in the pristine material, which means the interlayer distance along the *c*-axis was not totally recovered after being fully released, enabling a strong hybridization of the Pb/Bi 6s–6p and X p orbitals. As a result, a narrower band gap and wider visible light absorbance were achieved. Therefore, we believe that with the proper chemical atoms/ions, pressure can be used as a practical tool to lock-in the structure and physical properties in materials.

Transport properties and photocurrent

In situ high-pressure conductivity measurements were performed on $PbBiO_2Br$ using the quasi-four-probe methods within a DAC to better understand the pressure-tailoring electronic properties. Fig. 6a shows the electrical resistivity evolution of $PbBiO_2Br$ as a function of pressure upon compression and decompression. The initial high pressure was applied to ensure intimate contact between the powder sample and the Au contact leads. As the pressure increased, the resistivity dropped quickly by up to almost 3 orders of magnitude at 45 GPa. Usually, pressure can enhance the orbital overlap and increase the band dispersion, so the hybridization of the Pb/Bi-6s and O-2p orbitals could cause the monotonic decrease in resistivity.[24,32] After decompression, the structure changed back to a low-density state, leading to a reversible high resistance. Furthermore, as a reference, we also measured the resistance evolution of $PbBiO_2I$, which displayed similar behavior to that for the Br-based analog (see Fig. S5†). The conductivities of $PbBiO_2X$ improved significantly under extreme pressure, which may provide some novel application prospects in photoelectrochemical devices.

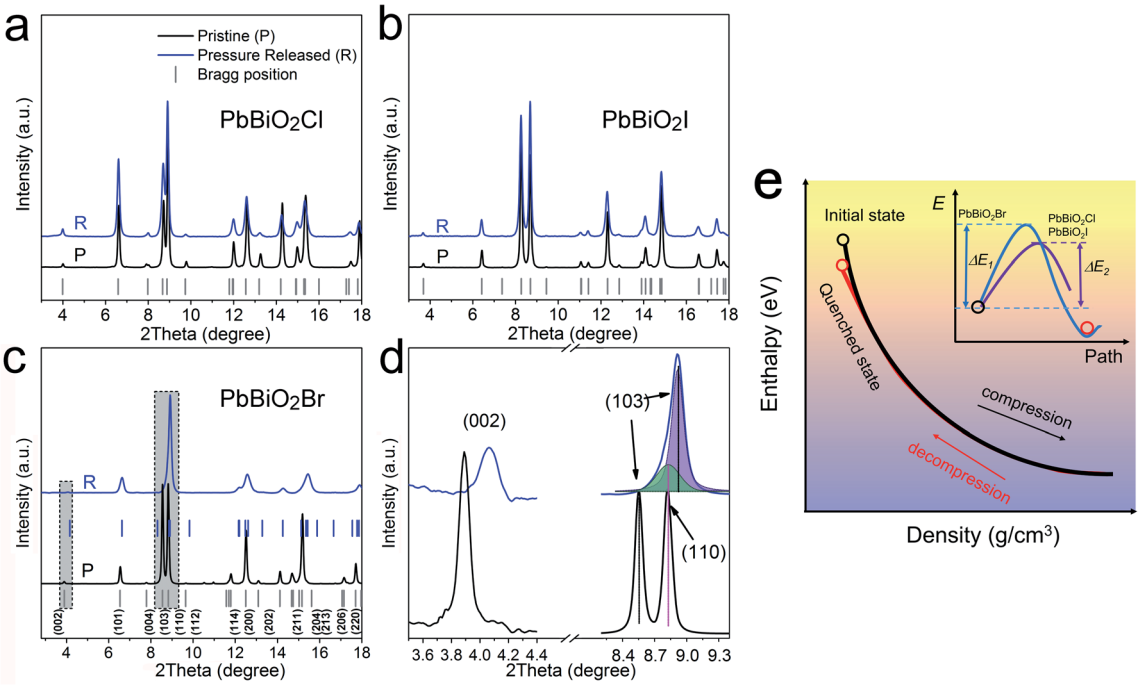

Fig. 5 (a–c) XRD comparison before and after high-pressure treatment up to 43 GPa for $PbBiO_2Cl$, $PbBiO_2Br$ and $PbBiO_2I$, respectively. P and R represent the pristine and after-pressure released samples. (d) Enlarged Bragg diffraction peaks (002), (103) and (110) from the hatched regions of (b). The broad peak around 8.9° after pressure releasing was fitted with two individual peaks. (e) The hypothesized enthalpy changes are driven by compression for $PbBiO_2X$. The reasonably small enthalpy difference ΔE_1 ($\Delta E_1 > \Delta E_2$) between the ground state and quenched state for $PbBiO_2Br$, leading to its retention structure and properties.

Another essential feature of photocatalysis with photoelectrochemical applications is photoresponsiveness. We evaluated the *in situ* transient photocurrent response for $PbBiO_2Br$ under the simulated solar illumination. As shown in Fig. 6b and c, $PbBiO_2Br$ exhibits a reproducible photocurrent response under high pressure, which follows swiftly with the light on and off, demonstrating the visible light activity and photochemical stability for our sample. The discernable photocurrent under high pressure from 28.7 GPa up to 43 GPa indicated a semiconductor feature as a photovoltaic/photocatalytic material. As the pressure increased, the photocurrent I_{ph} ($I_{ph} = I_{illuminated} - I_{dark}$) was indiscernible under ambient conditions, and was enhanced significantly to 21.5 μA (~48.6 mA cm^{-2} for ~140 mW cm^{-2} illumination) at 45.5 GPa. It was more than 4 orders of magnitude higher than the one reported at ambient pressure (~1.2 μA cm^{-2}).[27] This significantly enhanced photocurrent comes mainly from the remarkable enhancement in conductivity. As discussed above, structural changes under high pressure inherit the layered structural feature, which can explain the persistent photocurrent. As marked with the blue symbols and dashed line in Fig. 6d, the photocurrent reverted with decreasing pressure. In Sillen systems, the pressure-induced

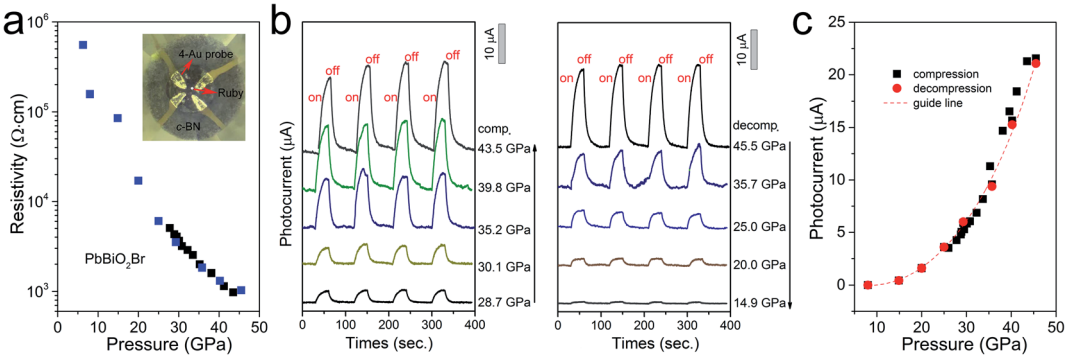

Fig. 6 (a) Resistivity of $PbBiO_2Br$ *versus* pressure during compression and decompression. Black and blue solid symbols represent the compression and decompression procedures, respectively. (b) Pressure-dependent transient photocurrent responses of $PbBiO_2Br$ under a visible light illumination for several light on–off cycles. (c) Photocurrent I as a function of pressure during compression and decompression.

switchable photoresponsiveness may be closely related to the reversible structure and resistance, and indicates its potential photocatalysis and applications as a switcher or controller.

It is well known that high-pressure research has made unprecedented progress in organic–inorganic halide perovskites by modifying the structure and properties, especially reducing the band gap toward more efficiency in harvesting solar energy for photovoltaic applications.[35] In this work, parallel band gap modulation has been successfully spread to complex bismuth-based semiconductors with a layered structure. More importantly, the pressure-induced structural and optical reversibility and irreversibility in Sillen X compound demonstrate a framework for understanding the in-depth structure–property relationships of Sillen compounds, and provide a new dimension for the rational design of semiconductors with tailored applications in optoelectronic/photoeletrochemical units.

Conclusions

Pressure and chemical engineering tools were applied to the layered semiconductors $PbBiO_2X$ (X = Cl, Br, I) in order to achieve better photoeletrochemical performance. Under compression, three $PbBiO_2X$ complexes underwent a robust tetragonal structural evolution, and presented an anisotropic compression behavior owing to their layered structural feature. $PbBiO_2X$ exhibited continuously narrowed band gaps under compression, which could be associated with the pressure-induced Bi–O bond shortening, and the distortion within the $PbBiO_2$ layer. Intriguingly, both crystal structures and band gaps of $PbBiO_2Cl$ and $PbBiO_2I$ were recoverable after pressure release. Conversely, $PbBiO_2Br$ showed partial irreversibility in both structural and optical properties. The probable mechanism of the irreversible behavior was also proposed, which was attributed to the unrecovered strains of bromide after pressure-treatment compared to the chloride and iodide analogs. A remarkably narrowed (2.52 eV, 4.5% drop) band gap of $PbBiO_2Br$ compared to the initial value under ambient conditions was obtained after the pressure was removed. By comparison of these three compounds, with the proper atomic size, some structure and optical properties can be locked-in on $PbBiO_2X$ through high-pressure processing. These findings highlight the synergistic effect of pressure and chemical engineering in optimizing the electronic and optical performances, providing new directions for further access to novel multifunctional materials.

Conflicts of interest

The authors declare no competing financial interest.

Acknowledgements

This work was financially supported by the National Nature Science Foundation of China (Grant No. 51527801, 51772184, U1930401) and Science Challenge Project No. TZ2016001. PX^2 program is supported by COMPRES under the NSF Cooperative Agreement EAR-1661511. APS is supported by DOE-BES, under Contract No. DE-AC02-06CH11357. The authors are also indebted to Dr H. Zhang, J. Liu, F. Zhang, H. Dong for their technical assistance with the UV-vis spectroscopy and XRD experiments.

References

1 H. Kageyama, K. Hayashi, K. Maeda, J. P. Attfield, Z. Hiroi, J. M. Rondinelli and K. R. Poeppelmeier, *Nat. Commun.*, 2018, **9**, 772.
2 G.-K. Ren, S.-Y. Wang, Y.-C. Zhu, K. J. Ventura, X. Tan, W. Xu, Y.-H. Lin, J. Yang and C.-W. Nan, *Energy Environ. Sci.*, 2017, **10**, 1590–1599.
3 X. Tan, J.-l. Lan, G. Ren, Y. Liu, Y.-H. Lin and C.-W. Nan, *J. Am. Ceram. Soc.*, 2017, **100**, 1494–1501.
4 L.-D. Zhao, J. He, D. Berardan, Y. Lin, J.-F. Li, C.-W. Nan and N. Dragoe, *Energy Environ. Sci.*, 2014, **7**, 2900.
5 H. Hiramatsu, H. Yanagi, T. Kamiya, K. Ueda, M. Hirano and H. Hosono, *Chem. Mater.*, 2008, **20**, 326–334.
6 A. M. Kusainova, W. Z. Zhou, J. T. S. Irvine and P. Lightfoot, *J. Solid State Chem.*, 2002, **166**, 148–157.
7 S. Liu, P. E. R. Blanchard, M. Avdeev, B. J. Kennedy and C. D. Ling, *J. Solid State Chem.*, 2013, **205**, 165–170.
8 A. M. Kusainova, P. Lightfoot, W. Zhou, S. Y. Stefanovich, A. V. Mosunov and V. A. Dolgikh, *Chem. Mater.*, 2001, **13**, 4731–4737.
9 A. M. Kusainova, S. Y. Stefanovich, V. A. Dolgikh, A. V. Mosunov, C. H. Hervoches and P. Lightfoot, *J. Mater. Chem.*, 2001, **11**, 1141–1145.
10 H. Kunioku, M. Higashi, O. Tomita, M. Yabuuchi, D. Kato, H. Fujito, H. Kageyama and R. Abe, *J. Mater. Chem. A*, 2018, **6**, 3100–3107.
11 H. Huang, S. Wang, Y. Zhang and X. Han, *Mater. Res. Bull.*, 2015, **62**, 206–211.
12 Z. Shan, X. Lin, M. Liu, H. Ding and F. Huang, *Solid State Sci.*, 2009, **11**, 1163–1169.
13 H. Kunioku, A. Nakada, M. Higashi, O. Tomita, H. Kageyama and R. Abe, *Sustainable Energy Fuels*, 2018, **2**, 1474–1480.
14 S. Füldner, P. Pohla, H. Bartling, S. Dankesreiter, R. Stadler, M. Gruber, A. Pfitzner and B. König, *Green Chem.*, 2011, **13**, 640–643.
15 H. Cheng, B. Huang and Y. Dai, *Nanoscale*, 2014, **6**, 2009–2026.
16 L. Ye, Y. Su, X. Jin, H. Xie and C. Zhang, *Environ. Sci.: Nano*, 2014, **1**, 90–112.
17 H. Suzuki, H. Kunioku, M. Higashi, O. Tomita, D. Kato, H. Kageyama and R. Abe, *Chem. Mater.*, 2018, **30**, 5862–5869.
18 J. Olchowka, H. Kabbour, M. Colmont, M. Adlung, C. Wickleder and O. Mentre, *Inorg. Chem.*, 2016, **55**, 7582–7592.
19 H. Fujito, H. Kunioku, D. Kato, H. Suzuki, M. Higashi, H. Kageyama and R. Abe, *J. Am. Chem. Soc.*, 2016, **138**, 2082–2085.
20 W. L. Mao, H.-k. Mao, P. J. Eng, T. P. Trainor, M. Newville, C.-c. Kao, D. L. Heinz, J. Shu, Y. Meng and R. J. Hemley, *Science*, 2003, **302**, 425–427.

21 Y. Ma, M. Eremets, A. R. Oganov, Y. Xie, I. Trojan, S. Medvedev, A. O. Lyakhov, M. Valle and V. Prakapenka, *Nature*, 2009, **458**, 182–185.
22 A. Jaffe, Y. Lin, W. L. Mao and H. I. Karunadasa, *J. Am. Chem. Soc.*, 2017, **139**, 4330–4333.
23 J. Zhao, L. Xu, Y. Liu, Z. Yu, C. Li, Y. Wang and Z. Liu, *J. Phys. Chem. C*, 2015, **119**, 27657–27665.
24 Q. Zhang, C. Chen, N. Li, Q. Huang, Y. He, X. Liu, B. Wang, D. Zhang, D. Y. Kim, Y. Wang, B. Xu and W. Yang, *J. Phys. Chem. C*, 2018, **122**, 15929–15936.
25 J. Ketterer and V. Krämer, *Mater. Res. Bull.*, 1985, **20**, 1031–1036.
26 D. O. Charkin, P. S. Berdonosov, V. A. Dolgikh and P. Lightfoot, *J. Solid State Chem.*, 2003, **175**, 316–321.
27 Y. Yu, S. Huang, Y. Gu, S. Yan, Z. Lan, W. Zheng and Y. Cao, *Appl. Surf. Sci.*, 2018, **428**, 844–850.
28 D. Zhang, P. K. Dera, P. J. Eng, J. E. Stubbs, J. S. Zhang, V. B. Prakapenka and M. L. Rivers, *J. Visualized Exp.*, 2017, 54660, DOI: 10.3791/54660.
29 C. Prescher and V. B. Prakapenka, *High Pressure Res.*, 2015, **35**, 223–230.
30 A. C. Larson and R. B. Von Dreele, *General Structure Analysis System (GSAS)*, Report LAUR, 86, 748, Los Alamos National Laboratory, Los Alamos, NM, 2004.
31 L. J. v. d. Pauw, *Philips Res. Rep.*, 1958, **13**, 1–9.
32 G. Zhang, Q. Zhang, Q. Hu, B. Wang and W. Yang, *J. Mater. Chem. A*, 2019, **7**, 4019–4025.
33 A. L. J. Pereira, D. Santamaría-Pérez, J. Ruiz-Fuertes, F. J. Manjón, V. P. Cuenca-Gotor, R. Vilaplana, O. Gomis, C. Popescu, A. Muñoz, P. Rodríguez-Hernández, A. Segura, L. Gracia, A. Beltrán, P. Ruleova, C. Drasar and J. A. Sans, *J. Phys. Chem. C*, 2018, **122**, 8853–8867.
34 V. S. Bhadram, L. Krishna, E. S. Toberer, R. Hrubiak, E. Greenberg, V. B. Prakapenka and T. A. Strobel, *Appl. Phys. Lett.*, 2017, **110**, 182106.
35 X. Lü, W. Yang, Q. Jia and H. Xu, *Chem. Sci.*, 2017, **8**, 6764–6776.
36 J. Zhao, L. Wang, D. Dong, Z. Liu, H. Liu, G. Chen, D. Wu, J. Luo, N. Wang, Y. Yu, C. Jin and Q. Guo, *J. Am. Chem. Soc.*, 2008, **130**, 13828–13829.
37 W. O. Uhoya, G. M. Tsoi, Y. K. Vohra, M. A. McGuire and A. S. Sefat, *J. Phys.: Condens. Matter*, 2011, **23**, 365703.
38 F. Birch, *Phys. Rev.*, 1947, **71**, 809–824.
39 D. Kato, K. Hongo, R. Maezono, M. Higashi, H. Kunioku, M. Yabuuchi, H. Suzuki, H. Okajima, C. Zhong, K. Nakano, R. Abe and H. Kageyama, *J. Am. Chem. Soc.*, 2017, **139**, 18725–18731.
40 D. J. Payne, R. G. Egdell, A. Walsh, G. W. Watson, J. Guo, P. A. Glans, T. Learmonth and K. E. Smith, *Phys. Rev. Lett.*, 2006, **96**, 157403.
41 A. Walsh, D. J. Payne, R. G. Egdell and G. W. Watson, *Chem. Soc. Rev.*, 2011, **40**, 4455–4463.
42 J. G. Cheng, K. E. Kweon, S. A. Larregola, Y. Ding, Y. Shirako, L. G. Marshall, Z.-Y. Li, X. Li, A. M. dos Santos, M. R. Suchomel, K. Matsubayashi, Y. Uwatoko, G. S. Hwang, J. B. Goodenough and J.-S. Zhou, *Proc. Natl. Acad. Sci. U. S. A.*, 2015, **112**, 1670–1674.
43 G. Liu, L. Kong, P. Guo, C. C. Stoumpos, Q. Hu, Z. Liu, Z. Cai, D. J. Gosztola, H.-k. Mao, M. G. Kanatzidis and R. D. Schaller, *ACS Energy Lett.*, 2017, **2**, 2518–2524.